


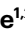








Ground magnetic survey on Mars from the Zhurong rover

Received: 18 July 2022

Accepted: 17 May 2023

Published online: 19 June 2023

 Check for updates

Aimin Du ^{1,2,15} ✉, Yasong Ge ^{1,2,15}, Huapei Wang ^{3,15}, Haiying Li⁴, Ying Zhang ^{1,2}, Hao Luo^{1,2}, Can Huang ^{1,2}, Lican Shan ^{1,2}, Fei Han³, Yang Liu ⁵, Yongliao Zou⁵, Chi Wang ⁵, Yongxin Pan^{2,6}, Qingsong Liu⁷, Ross N. Mitchell ^{2,8}, Yang Jia⁹, Baichao Chen⁹, Shengyi Jin⁹, Yi Jiang¹⁰, Tielong Zhang^{11,12,13}, Rixiang Zhu^{2,8}, David Gubbins¹⁴ & Keke Zhang ¹⁰ ✉

Mars' magnetic field has been measured at large scale by orbiting spacecraft and at very small scale via Martian meteorites. Here we report on a ground magnetic survey on metre to kilometre scales. The Zhurong rover made vector measurements at 16 sites along a 1,089 m track in the Utopia Basin on Mars. It recorded an extremely weak magnetic field, with an order of the average intensity less than that inferred from orbit, in contrast to the large magnetic field in Elysium Planitia measured by InSight. A spacecraft measurement samples an area with radius comparable to its altitude, while a ground measurement samples an area with radius comparable to the depth of the magnetized body. The weak magnetic field measured by Zhurong indicates no magnetization anomalies for a depth of many kilometres around and below the rover's traverse. We suggest two possible explanations for the weak magnetic field: the entire Utopia Basin may have remained unmagnetized since its formation about 4 billion years ago or that the 5-km-radius ghost crater where Zhurong landed may have been demagnetized by impact.

Measurements of crustal magnetic fields of terrestrial planets provide crucial insights into their core dynamo history and interior thermal evolution. Unlike Earth, Mars is found to have no global magnetic field today, but heterogeneous and locally strong crustal magnetization, indicating the existence of an ancient dynamo¹. Magnetic surveys probe crustal magnetism on length scales comparable to

the distance, or altitude, from the source². The Mars Global Surveyor spacecraft mapped Mars' magnetic field globally at 185 km (magnitude only)³ and 400 km (vector field), though locally as low as 90 km (ref. 4) showing magnetic fields up to 1,500 nT. The Mars Atmosphere and Volatile Evolution (MAVEN) spacecraft extended global vector magnetic field mapping down to 150 km (refs. 5,6). At the other end

¹CAS Engineering Laboratory for Deep Resources Equipment and Technology, Institute of Geology and Geophysics, Chinese Academy of Sciences, Beijing, China. ²College of Earth and Planetary Sciences, University of Chinese Academy of Sciences, Beijing, China. ³Paleomagnetism and Planetary Magnetism Laboratory, School of Geophysics and Geomatics, China University of Geosciences, Wuhan, China. ⁴National Astronomical Observatories, Chinese Academy of Sciences, Beijing, China. ⁵State Key Laboratory of Space Weather, National Space Science Center, Chinese Academy of Sciences, Beijing, China. ⁶Key Laboratory of Earth and Planetary Physics, Institute of Geology and Geophysics, Chinese Academy of Sciences, Beijing, China. ⁷Centre for Marine Magnetism, Department of Ocean Science and Engineering, Southern University of Science and Technology, Shenzhen, China. ⁸State Key Laboratory of Lithospheric Evolution, Institute of Geology and Geophysics, Chinese Academy of Sciences, Beijing, China. ⁹Beijing Institute of Spacecraft System Engineering, Beijing, China. ¹⁰State Key Laboratory of Lunar and Planetary Sciences, Macau University of Science and Technology, Macau, China. ¹¹Harbin Institute of Technology, Shenzhen, China. ¹²Chinese Academy of Sciences Center for Excellence in Comparative Planetology, Hefei, China. ¹³Space Research Institute, Austrian Academy of Sciences, Graz, Austria. ¹⁴School of Earth and Environment, University of Leeds, Leeds, UK. ¹⁵These authors contributed equally: Aimin Du, Yasong Ge, Huapei Wang. ✉e-mail: amdu@mail.iggcas.ac.cn; K.Zhang@exeter.ac.uk

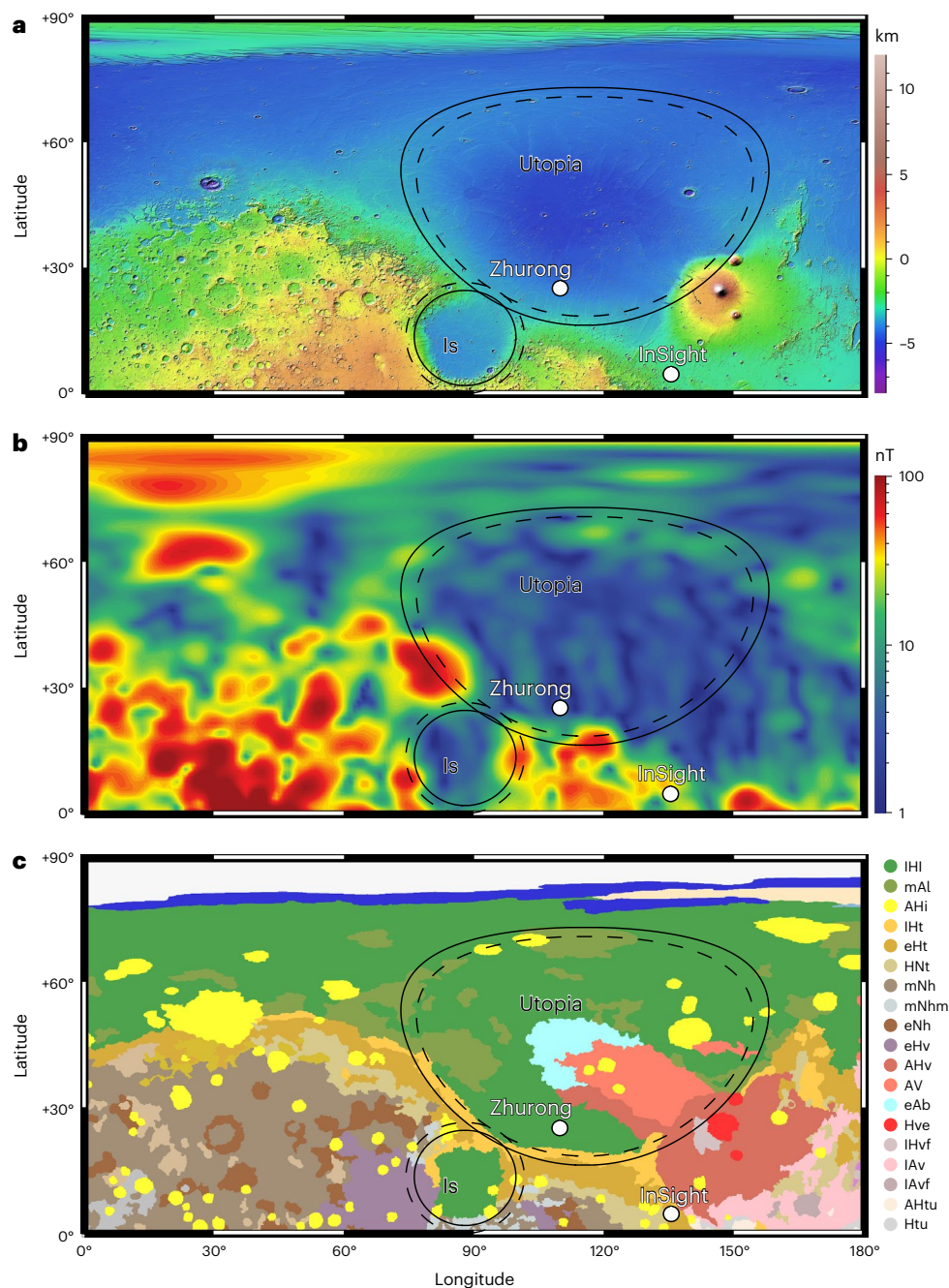


Fig. 1 | Maps of Mars near the landing site in Mercator projection. a, Mars Orbiter Laser Altimeter topography⁴⁷. The rover landed in the southern Utopia Basin (marked) at 25.066° N, 109.926° E, northwest of the InSight landing site. **b,** The modelled total magnetic field strength at an altitude of 200 km (ref. 14). **c,** The corresponding geologic map⁴⁸ whose key for the colours and

geologic units is provided as Supplementary text. Note that resurfacing events in localized areas, such as around the Zhurong landing site, were not indicated in this standard geologic map. Major impact basin boundaries of Isidis (Is) and Utopia are shown with solid black (topography^{49,50}) and dashed black (demagnetization²¹) lines.

of the spectrum, palaeomagnetic analyses of samples from a Martian meteorite (ALH84001) revealed evidence of the ancient magnetic field at very small length scales (~1 mm), supporting the operation of an early Martian dynamo before 4.1 Ga or possibly 3.9 Ga (ref. 7). However, the origin of Martian crustal magnetization and the history and attributes of the ancient dynamo remain topics of active interest. Many of the outstanding key questions require new high-resolution regional data sets such as local magnetic field measurements⁸. The NASA InSight fluxgate magnetometer (IFG) measured the ground-level magnetic field at a single landing site⁹. The surface magnetic intensity (~2,000 nT) measured by IFG is very high by the standard of a terrestrial crustal field

(typically <200 nT)¹⁰ but can be accounted for by natural variations in Mars' mineralogy and/or thick lithosphere. Metre-to-kilometre scale regional surveys are particularly critical for investigating the characteristics of the subsurface magnetic mineralogies as well as the geological structures. This can, in turn, constrain the timing and evolution of the Martian dynamo⁸. What has been missing so far are magnetic measurements on the length scale most useful to geologists and geophysical prospectors, that is, the kilometre-scale ground survey.

The Zhurong rover landed in the southern Utopia Basin (Fig. 1) on 15 May 2021 and carried out a magnetic survey in the 3 months after landing. The Mars Rover Magnetometer (RoMAG)¹¹ scientific payload

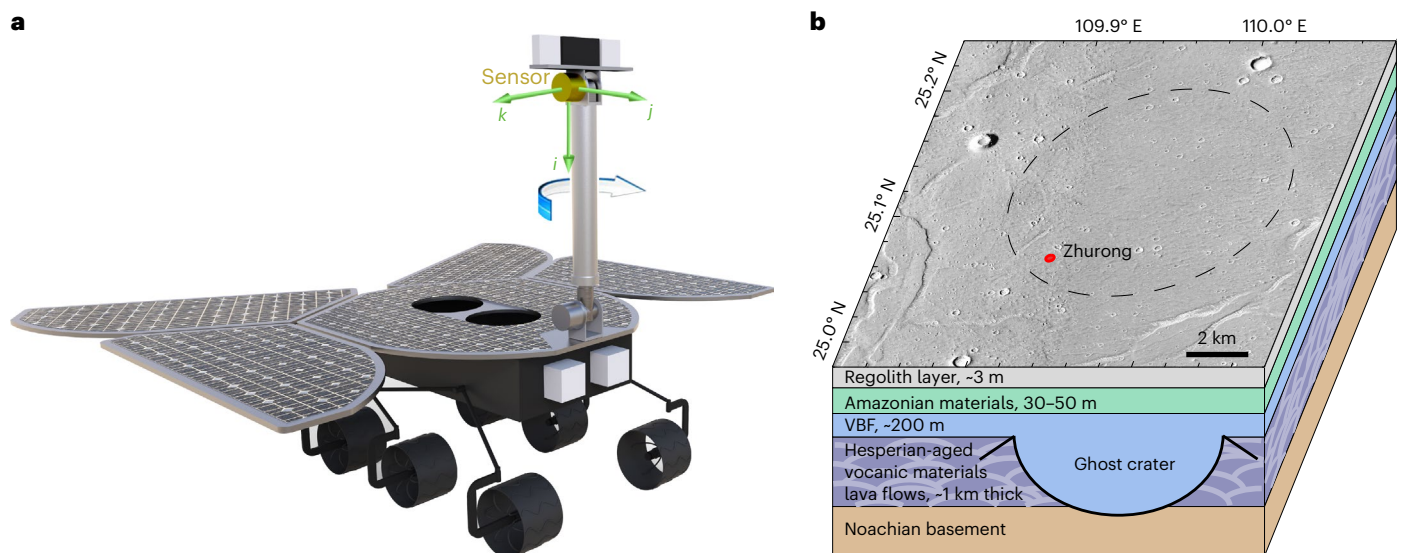


Fig. 2 | The Zhurong rover and the relevant geologic context. **a**, The Zhurong rover (with dimensions of approximately 3.3 m × 3.2 m × 1.85 m) and its two three-component fluxgates¹¹, one at the top of the mast, which can rotate, and a fixed one at the intersection of the mast and the rover deck. **b**, The CTX image of

Zhurong's landing site (https://www.nasa.gov/mission_pages/MRO/spacecraft/sc-instru-ctx.html) and the inferred stratigraphy with estimated layer thickness and a ghost crater beneath Zhurong's landing site (red dot), with the black dashed circle marking the ghost crater previously identified^{12,13}.

onboard the Zhurong rover consists of two identical tri-axial fluxgate magnetometers (Fig. 2a) with a dynamic range of $\pm 65,000$ nT, a noise level at 0.01 nT/ $\sqrt{\text{Hz}}$ @ 1 Hz. One is mounted on the mast, and the other at the intersection of the mast and the rover deck. The upper fluxgate can rotate about a vertical axis. The horizontal magnetic field associated with the rover is removed by rotating the upper fluxgate while keeping the lower one fixed and by repeating the process with the rover pointing in different directions. It should be noted, however, that it is not possible to calibrate the vertical component in this way, so only the horizontal components are discussed in this paper.

The RoMAG measures a combination of the internal fields, rover-generated interference and the external fields. The convention in geomagnetism is to refer to the crustal magnetic field (and core dynamo-generated field where one exists) as 'internal' and those originating in the upper atmosphere and beyond (ionosphere, magnetosphere, Sun, etc.) as 'external'. In this study, rover-generated fields were removed by a two-step calibration method, and the external contribution of the measurements is estimated using observations from the InSight lander and an ionospheric dynamo model (Methods).

Results

Magnetic measurements in this survey were made at 16 locations along a 1,089 m track during 90 sols from 4 June to 3 September 2021 (Extended Data Fig. 1) in a small ghost crater^{12,13} of about 5 km in radius (Fig. 2b) whose centre is located at 25.12° N, 109.97° E. The calibration process, which involves the mast rotations and rover rotations, was conducted to derive the Martian field along its traverse (Extended Data Figs. 2 and 3). The measured magnetic fields of crustal origin were then acquired by removing the external contribution from the Martian fields at the 16 locations (Extended Data Fig. 4). The track of the magnetic survey is depicted in Fig. 3a, and the results of the crustal fields are presented in Fig. 3b–d. The directions of the estimated crustal magnetic field are predominantly southeast. The amplitudes of the north–south horizontal component typically range from 3.4 to 24.0 nT after removing the external field and contributions from the rover itself (Methods). The total intensity, which excludes the uncalibrated vertical component, ranges from 5.2 to 39.8 nT, while the average of horizontal intensities is 11.2 nT with a standard deviation of 10.9 nT. The measurements show a significant variation of the surface field

in magnitude and direction along the Zhurong traverse. In the first segment (about 0–200 m, sols 21–50) of the traverse, the magnetic field is extremely weak (<10 nT) and close to zero. In the second segment (about 200–600 m, sols 58–79), the magnetic field is moderately weak at about 30 nT. In the final segment (about 600–1,000 m, sols 87–110), the magnetic field becomes extremely weak again (<10 nT) and close to zero. This suggests that the Zhurong rover landed in an area of exceptionally low magnetic field and that the scale size of the local magnetization is on the order of several hundred metres, which can only be revealed via a ground magnetic survey. One should bear in mind that some, or even all of, the variations may be due to ionospheric contributions that deviate from those estimated in this paper (Methods). The possibility of zero magnetization beneath Zhurong's traverse exists in this sense.

The intensities of the magnetic field measured by RoMAG are much smaller than estimates from the latest orbital data-based model¹⁴ (we shall sometimes refer to ref. 14 as L19 herein) downwards continued to the planet's surface (intensity of 81 nT and horizontal intensity of 55 nT). By contrast, NASA InSight's single-site measurement on Elysium Planitia was about ten times stronger than the orbital prediction (about 300 nT)⁹. The very low values at the Zhurong magnetic survey region are also unlikely to be found in the crustal field of many places on Earth, particularly above volcanics containing magnetic minerals. However, on Mars, there is no induced magnetization because there is no dynamo field at present. Remanence may be absent because of demagnetization or because the rocks were formed after dynamo action ceased.

Zhurong's landing site lies in a geologically simple terrain within the giant impact basin Utopia Planitia in the Northern Hemisphere, where the overall magnetic field is weak^{15,16}. The surface of the basin is exceptionally smooth with low crater density, which indicates a surface age of Hesperian to Amazonian¹⁷. The inferred stratigraphic structure (Fig. 2b) shows that the ancient Noachian basement at a depth of several kilometres has been flooded and filled with Hesperian-aged volcanic lavas with a 1–2 km thickness. The late Hesperian-aged Vastitas Borealis Formation (VBF) sediments, interpreted to be the residue of outflow channel effluents derived from the southern highlands or as a sublimation residue of the putative ocean, have been emplaced on the volcanic Hesperian plain. It is also evident that resurfacing has occurred in the landing area in the middle Amazonian (that is, ~ 1.6 Ga), which may

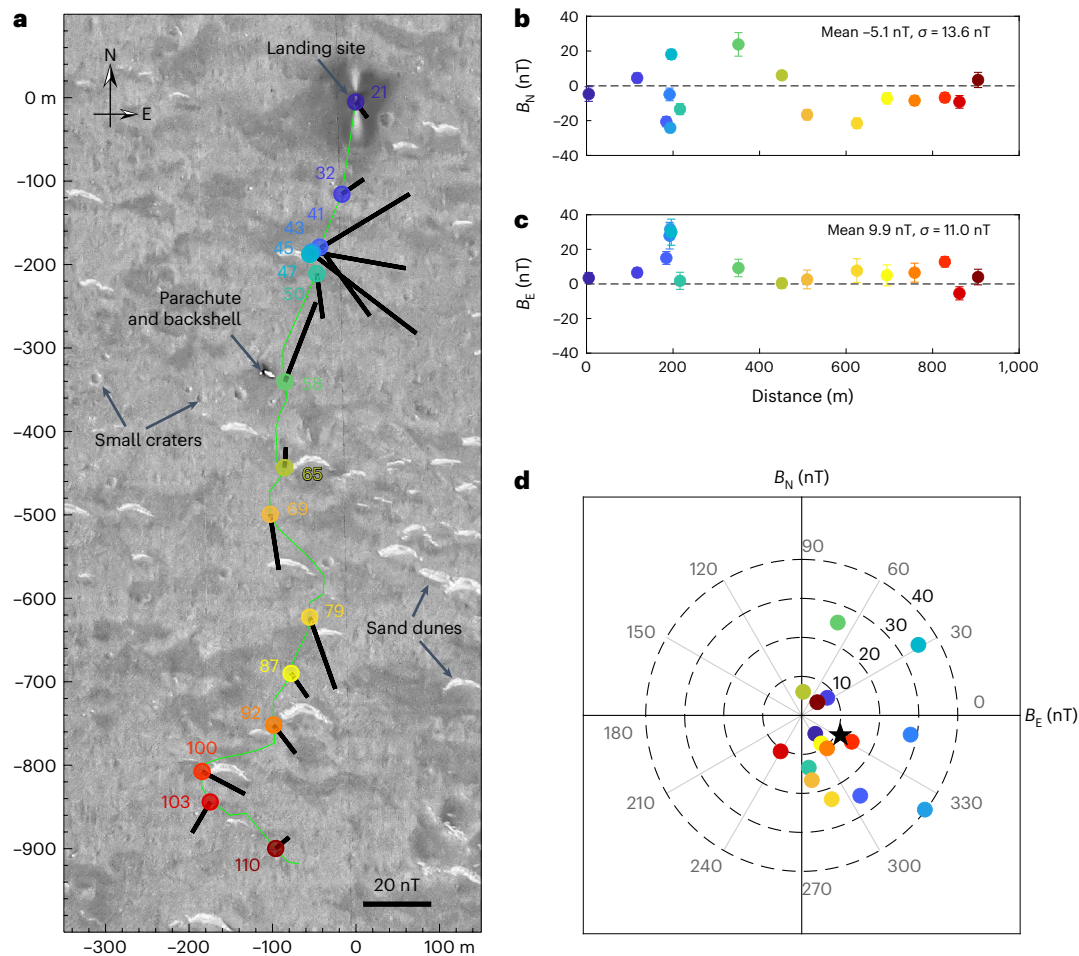


Fig. 3 | RoMAG measurements along the Zhurong traverse. **a**, Measured horizontal magnetic fields components of crustal origin at 16 sites along the Zhurong traverse overlaid on an image of surface features from Tianwen-1's high-resolution imaging camera. Coloured dots and numbers show the locations and the sols of magnetic observations, respectively. Black lines indicate horizontal components of the magnetic vector. The values of the measurements along the Zhurong traverse at 16 sites are shown in Extended Data Fig. 4.

b,c, The northwards (**b**) and eastwards (**c**) magnetic component at 16 observation points in the geographic frame of Mars. The error bar overlotted on each of the 16 points is the uncertainty calculated from the error propagation (Extended Data Fig. 4). **d**, The distribution of horizontal components in the geographic frame of Mars. The black star marks the vector mean of the horizontal fields at 16 locations. Colour codes in **a–d** are the same.

represent a volcanic flooding event. Crater counting analysis indicates that the filling of VBF and volcanic materials could have transformed Hesperian craters into ghost craters by 3.45 Ga (ref. 18). Zhurong rover radar has revealed Amazonian material tens of metres thick, covered with a regolith layer several metres thick¹⁹.

Discussion

A straightforward way of explaining an extremely weak magnetic field measured by the Zhurong rover is that the entire Utopia Basin, and the crust beneath it, may have remained unmagnetized since the formation of the Utopia impact basin about 4 billion years ago²⁰ and that the landing site is representative of surrounding area. The demagnetization radius of the Utopia impact is estimated to be 1,600 km, and the distance of the Zhurong landing site to the impact basin centre is about 1,200 km (ref. 21). In other words, the Zhurong measurements were made within a large, demagnetized region in Utopia Basin. The lack of strong magnetic signals above the large impact basins from orbital altitude is obvious. However, up to now, it could not unambiguously be argued that the field is close to zero on the surface. The Martian surface fields measured by Zhurong impose a strong constraint on the remagnetization processes of the crust underlying

Utopia Basin after the region was pervasively demagnetized by the giant basin-forming impact²¹.

Since negligible subsequent demagnetization is expected from burial by post-dynamo lavas²² or younger sediments, the extremely weak surface fields from RoMAG measurements suggest that the Hesperian lava flows were never magnetized and that the dynamo may have ceased at or before the original Utopia basin-forming impact in the Noachian. Alternatively, demagnetization associated with the impact in the presence of a dynamo field has been suggested²³. Further, the possibility remains that the region near RoMAG was demagnetized by a later sizeable impact whose signature is buried. This possibility is discussed below.

Another way of explaining an extremely weak magnetic field measured by the Zhurong rover is that the 5-km-radius ghost crater^{12,13} where Zhurong landed was demagnetized by the impact that formed the original crater. Ghost craters are impact craters that have been buried by younger materials such as lavas or sediments. They are often identified by circular structures in the overlying materials, typically in the form of concentric double grabens thought to be formed from compaction around the inferred rim of the buried crater¹². The double-ringed structure in the Zhurong landing region (Extended Data Fig. 5a) suggests

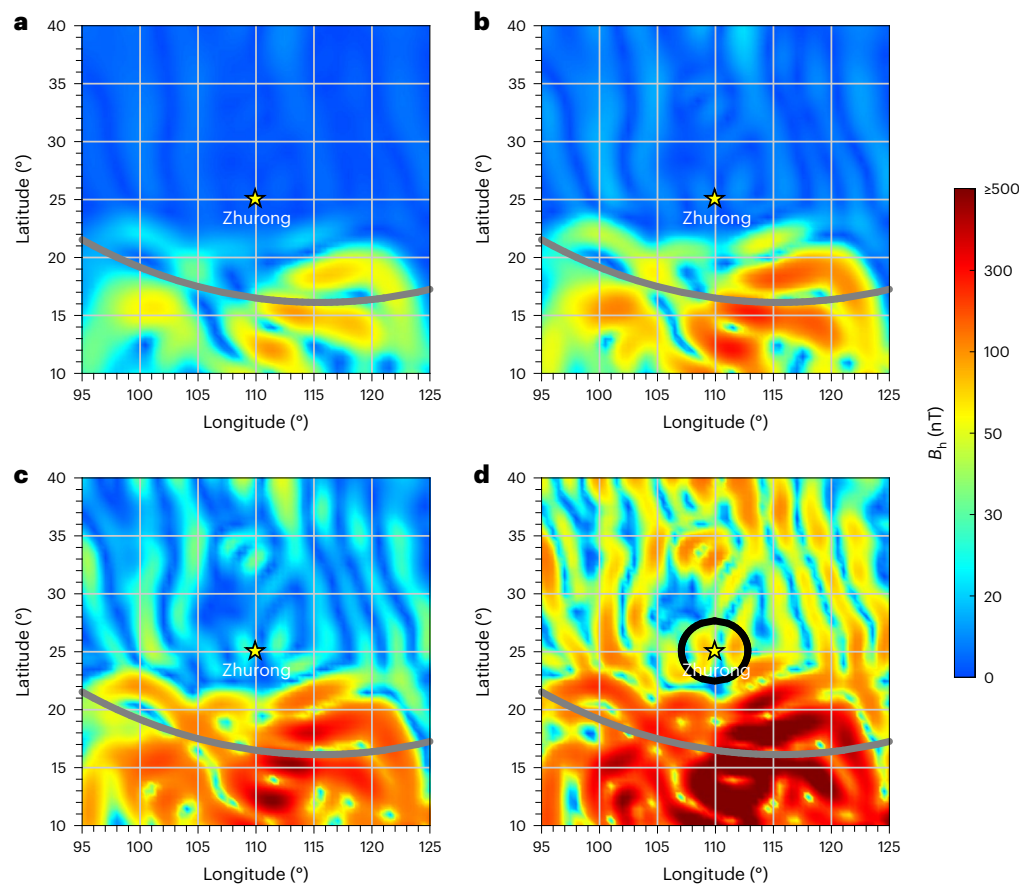


Fig. 4 | The satellite-based magnetic field model (L19) and areas influenced by measurements. **a–d**, Maps of the horizontal magnetic field strength in the Zhurong landing region predicted by the L19 model¹⁴ downwards continued to four different heights of $h = 150$ km (**a**), 100 km (**b**), 50 km (**c**) and 0 km (**d**). The corresponding field strength at the Zhurong landing site (25.066° N, 109.926° E; star) is approximately 2.6 nT at $h = 150$ km, 5.6 nT at $h = 100$ km, 16.2 nT at

50 km and 55.1 nT at the Martian surface. The black circle at $h = 0$ km denotes the approximate ground area averaged by the orbital model with a radius of 150 km. It includes some of the stronger anomalies. The corresponding circle for Zhurong's ground measurement, assuming a magnetized layer of depth 1 km, is too small to be shown on this scale. The grey curve indicates the topography boundary of Utopia Basin at the surface altitude.

that the landing site is $1\text{--}2$ km from the rim of the ghost crater¹³, which may have been formed from an impact that penetrated the Hesperian lava units, subsequently buried by VBF (Fig. 2b).

How can one explain the difference between the Zhurong measurements and orbital predictions at ground level? Satellite measurements resolve length scales that are 100 times more than the Zhurong's traverse. Either Zhurong landed in an area of exceptionally low magnetization, or the orbital predictions represent the limit of accuracy of the downwards continued magnetic field. If the former, the low-magnetization region could be the ghost crater demagnetized by impact. If the latter, the $50\text{--}100$ nT prediction could be the result of amplification of errors by the downwards continuation process, which is particularly large for the harmonics of highest degree. The problem of assessing the detailed interpretation of orbital fields at ground level for Utopia and other basins will form a separate future study.

Next, we investigate possible sources of crustal magnetization that would be detectable by the Zhurong rover. The satellite field is often downwards continued to ground level to give an average of the surface field when in situ surface observations are unavailable. This method has the advantage of generality, being independent of the depth of any magnetic source, but it is well known that a magnetic field model constructed from orbital data cannot reliably predict the surface magnetic field strength at a point. Downwards continuation can be viewed by accumulating contributions from an area of interest and with different weights determined by the relevant

Green's function for the Laplacian^{24,25}. The area of interest is where the weighting is significant, a circle with a radius of order the altitude of the satellite (150 km). Figure 4a–d shows the horizontal magnetic field (see Extended Data Fig. 6 for the corresponding vertical magnetic field) from L19 downwards continued to different altitudes, with a circle denoting the area of significant weighting. It should be highlighted that magnetic fields at orbital altitudes are dominated by wavelengths of crustal magnetism that are comparable to the distance from the source². Downwards continuation of a model from this altitude will thus necessarily miss the shorter-wavelength components that dominate the surface field. Given that the L19 model includes data between 120 and 170 km, these wavelengths (clearly visible in the patterns in Fig. 4) dominate the predicted field at the surface. The crustal magnetic field intensity predicted by the L19 model at 150 km is about 5 nT, which is less than the MAVEN r.m.s. misfit (-9.42 nT). Thus, the crustal field in the L19 model may be primarily noise and consistent with either zero or extremely small crustal magnetic fields at orbital altitude. If there is strong but small-scale magnetization (say, <10 km) around Zhurong's traverse, this will not be clearly visible at orbital altitudes but could cause very strong surface magnetic fields. This is likely the case for the InSight landing site. However, if there is weak or zero crustal magnetization in the region, the surface magnetic field will of course be weak, and the orbital field will also be weak and dominated by non-crustal noise which will be amplified when downwards continued to the surface.

A helpful way of understanding the RoMAG measurements is to construct a specific magnetic forwards model of the ghost crater, which has been buried by younger materials such as lavas or sediments. The ghost crater model has the advantage of specificity. It provides an upper-limit estimation of the crust magnetization beneath the landing site constrained by the Zhurong surface measurements. We constructed a forwards model with a weakly magnetized uniform layer (with dimensions of 1,000 km \times 1,000 km \times 1 km; north, east and vertical components of magnetization $M_N = 0 \text{ A m}^{-1}$, $M_E = 0.1 \text{ A m}^{-1}$ and $M_Z = 0.1 \text{ A m}^{-1}$, respectively) representing the layer of Hesperian lava flows. A cylindrical hole was placed in the centre to represent the ghost crater that penetrated the lava layer (Extended Data Fig. 5b, lower panel). The horizontal magnetic field is very weak ($\sim 6 \text{ nT}$) at 200 m above the crater centre, as predicted by the forwards model. The strongest horizontal strength (up to 41 nT) along the rim of the hole (Extended Data Fig. 5b, middle panel) is comparable to the maximum strength of the value observed by Zhurong. The weak magnetic field shown by this forwards model is consistent with the crust beneath the Zhurong landing region, which is weakly magnetized at about 0.14 A m^{-1} (magnitude of magnetization of the uniform layer). The magnitude is likely to represent an upper limit of the crust magnetization beneath the Zhurong rover that is far less than the magnetization of the Southern Hemisphere ($\sim 10 \text{ A m}^{-1}$)²⁶.

The crustal magnetic fields of Mars have been critical in dating the duration and timing of its ancient dynamo^{26–29}. Nonetheless, challenges and unsolved problems remain. The interpretation so far has necessarily been simplistic, with absence of magnetic anomalies indicating structures that were either never magnetized because they were formed when the dynamo was inactive, were subsequently demagnetized by impact or other alteration, or buried by deep, younger lavas erupted when the dynamo was inactive. Virtually all the magnetic interpretation up to now has come from satellites some 150 km or more above the surface of Mars, limiting the spatial resolution to worse than 100 km. It is not surprising, therefore, that satellite predictions are different from point surface measurements because spatial variability on small length scales and/or weak magnetization cannot be captured.

Zhurong's weak values can similarly be explained as natural variations. However, the model derived from orbital magnetic field data predicts anomalies of about 73 nT, which are much larger than the $\sim 10 \text{ nT}$ recorded by Zhurong. They could arise from deeper layers that were magnetized at formation. It is possible that an ancient dynamo was operating when the dichotomy formed²⁷ and some of the weakly magnetized basement was preserved after the Utopia Basin impact. Any new lava flows could be magnetized by the underlying anomalies and would otherwise mask the deeper anomalies. Our crater model requires weak magnetization of the sort that could result from the basin-forming impact, owing to either the absence of a magnetic field during formation¹ or processes associated with the impact such as excavation²⁷ or cooling in a polarity-changing dynamo field²³. Indeed, weak or zero magnetization that could occupy most of Utopia Planitia could easily come from the impact that formed the basin, which occurred under the hypothesis that there was no global dynamo magnetic field at that time. Indeed, the magnetization of the highly magnetizable early Hesperian lavas had to already have been weak before the impact that formed the ghost crater, which may provide further constraints on the evolution of the Martian dynamo.

We have started ground magnetic surveys on Mars and entered a new era of more detailed interpretation, using scientific methods similar to those successfully employed for ground magnetic surveys on Earth over the last 100 years. The landing site in a ghost crater is indeed fortunate because, unlike an exposed crater with a steep rim that is potentially hazardous to cross, Zhurong may be able to drive over the outer rim and observe magnetic anomalies that are larger than seen so far. The original 90-sol mission has been completed, but Zhurong is

capable of more exploration. In our preliminary extended mission plan, Zhurong will be deployed by further southwards travel of about 20 km, approaching and crossing the outer crater rim and visiting other small volcanic features that may have stronger magnetic anomalies. These would fill the gap in our knowledge on the magnetization of smaller craters and, more importantly, the processes by which all craters are magnetized and demagnetized.

Together with Tianwen-1 orbital observations of space magnetic fields and plasma environments, the Zhurong RoMAG further surface measurements will offer an extraordinary opportunity to study the history of the Martian environment. Concurrent observations between Zhurong RoMAG and InSight IFG may be essential to elucidate the variations of ionospheric currents at different local times and to identify sources of time-varying magnetic fields.

Methods

Instrument and operation modes

Full details of the RoMAG instrumentation can be found in a previous study¹¹. The RoMAG is a set of magnetometers with two identical tri-axial fluxgate sensors, one mounted near the top of the mast of the Zhurong rover, and the other fixed on the mast base. The fluxgate magnetometers measure magnetic fields with a dynamic range of $\pm 65,000 \text{ nT}$ with a noise level of $0.01 \text{ nT}^{-1/2}$ at 1 Hz, and a normal sample rate of 1 Hz and capacity of 32 Hz in burst mode. The first RoMAG measurements were implemented in the rover static mode on 4 June 2021, which occurred at the first observation point, 5.14 m away from the lander. During the following 90 sols, RoMAG acquired raw data of magnetic vector fields at another 15 observation points over a total distance of 1,089 m.

After stopping at the first observation point, the rover started science operations. The starting time and operation sequence on 5 June 2021 are presented in Supplementary Table 1. During the period of mast rotation, RoMAG was the only instrument operating. The same operation sequence was conducted at all 16 observation points, except for slightly different angles and durations for each yaw rotation of the mast (Extended Data Fig. 1). In addition to the 16 regular explorations, we conducted an along-track calibration (Supplementary Table 2) on 5 January 2022 for one time, during which both the mast and rover rotations were implemented at a fixed location to make a cross calibration. The whole along-track calibration process lasted about 1 h, and the RoMAG was also the only instrument operating.

Removal of rover fields and determination of Martian fields

The measured magnetic fields (\mathbf{B}_o) were the sum of three contributions: the ambient field (\mathbf{B}_{Mars}), the field originating from the rover mast system (\mathbf{B}_{mast}) and the field generated by the rover body (\mathbf{B}_{body}) including fields from solar array currents. To determine \mathbf{B}_{Mars} , we selected data during periods of mast rotations to remove rover fields from the RoMAG measurements that had been processed through a calibration procedure. We only deal with the observed magnetic fields from the top sensor as the bottom one did not rotate with the mast. In addition, owing to the closer distance to the rover body and the mast rotation motor, the dynamic interferences in the bottom sensor were apparently stronger than for the top one, especially during the mast rotations (not shown). Therefore, below we determine the Martian fields based only on the measurements from the top sensor.

It was shown that the measured magnetic field (\mathbf{B}_o) is on the order of $\sim 10,000 \text{ nT}$ and varies by several hundred nanotesla for each detection. The Multispectral Camera (MSCam), which is also mounted on the mast, is quite close to the top sensor. Although the MSCam is switched off during the mast rotation, magnetic fields from the permanent magnet in the MSCam primarily contribute to the measured magnetic field. There is a steering mechanism that controls the pitch angle of the camera. The pitch angle varies at different detection locations to get a better view, but it does not vary during the mast rotation. Therefore, the

magnetic fields generated by the permanent magnet remain steady during the mast yaw rotation, but vary for each measurement at different sites owing to the change of the pitch angle of the camera. For each mast rotation, \mathbf{B}_{Mars} (Mars geographic frame), \mathbf{B}_{body} (rover frame) and \mathbf{B}_{mast} (sensor frame) are constants and can be sufficiently separated by using a simple analytical model with relative sensor rotations, as is common practice in the in-flight calibration of fluxgate magnetometer offsets^{5,30,31}. We construct a two-step procedure to separate the three fields using manoeuvres of the mast and the rover. When the mast rotates around its z axis, the \mathbf{B}_{mast} in the sensor frame and the combined field (\mathbf{B}_{Mars} and \mathbf{B}_{body}) in the rover frame are constants (Extended Data Fig. 2a). The field vector rotations generate smooth variations in their horizontal components (B_j, B_k) that are recorded by the RoMAG sensor (Extended Data Fig. 2c), which is presented as a circular rotation in the hodograph of $B_j - B_k$ (Extended Data Fig. 2d). Using a similar method, we can further separate \mathbf{B}_{Mars} and \mathbf{B}_{body} using horizontal rotations of the whole rover, in which only \mathbf{B}_{Mars} changes its direction in the rover frame (Extended Data Fig. 2b). Considering that the rover rotation was only done once on 5 January 2022, it has to be replaced by comparing the relative changes of the rover's heading directions at observation points in the regular detection, as the RoMAG was conducting measurements only when the rover was still.

To be specific, by assuming that the combined field (\mathbf{B}_c) of \mathbf{B}_{Mars} and \mathbf{B}_{body} near the sensor does not vary during the mast rotation, the observed magnetic field \mathbf{B}_o in the frame of the rotating sensor can be expressed with a linear equation as

$$\mathbf{B}_o = C \times \mathbf{B}_c + \mathbf{B}_{\text{mast}}, \tag{1}$$

where \mathbf{B}_{mast} is in the sensor frame (i, j, k), \mathbf{B}_c is in the rover frame (x, y, z) and C is the rotation matrix defining the transformation from the rover frame to the sensor frame, given by

$$C = \begin{bmatrix} 0 & 0 & -1 \\ 1 & 0 & 0 \\ 0 & -1 & 0 \end{bmatrix} \times \begin{bmatrix} 1 & 0 & 0 \\ 0 & \cos \alpha & \sin \alpha \\ 0 & -\sin \alpha & \cos \alpha \end{bmatrix} \times \begin{bmatrix} \cos \beta & 0 & -\sin \beta \\ 0 & 1 & 0 \\ \sin \beta & 0 & \cos \beta \end{bmatrix} \times \begin{bmatrix} \cos \gamma & \sin \gamma & 0 \\ -\sin \gamma & \cos \gamma & 0 \\ 0 & 0 & 1 \end{bmatrix}, \tag{2}$$

where the Euler angles α, β and γ describe this transformation based on a z - y - x rotation sequence and γ is the mast rotation angle. As the sensor rotates with the z axis, C can be simplified to

$$C = \begin{bmatrix} 0 & 0 & -1 \\ 1 & 0 & 0 \\ 0 & -1 & 0 \end{bmatrix} \times \begin{bmatrix} \cos \gamma & \sin \gamma & 0 \\ -\sin \gamma & \cos \gamma & 0 \\ 0 & 0 & 1 \end{bmatrix}, \tag{3}$$

then equation (1) can be rewritten as

$$\begin{cases} B_{o,i} = -B_{c,z} + B_{\text{mast},i} \\ B_{o,j} = B_{c,x} \cos \gamma + B_{c,y} \sin \gamma + B_{\text{mast},j} \\ B_{o,k} = B_{c,x} \sin \gamma - B_{c,y} \cos \gamma + B_{\text{mast},k} \end{cases}, \tag{4}$$

where the subscripts i, j, k and x, y, z denote corresponding components of the sensor frame and the rover frame, respectively.

Moving $B_{\text{mast},j}$ and $B_{\text{mast},k}$ in the second and third equations in equation (4) to the left-hand side respectively, squaring both sides and adding the two equations together, we get

$$(B_{o,j} - B_{\text{mast},j})^2 + (B_{o,k} - B_{\text{mast},k})^2 = B_{c,x}^2 + B_{c,y}^2. \tag{5}$$

This equation represents a circle, where $(B_{\text{mast},j}, B_{\text{mast},k})$ are the coordinates of the centre of the circle in the $B_j - B_k$ plane and $\sqrt{B_{c,x}^2 + B_{c,y}^2}$ is the radius.

Expanded equation (1), we can reduce the problem to a linear multivariable equation below and solve it by the least-squares method as follows:

$$\begin{pmatrix} C_{11}^1 & C_{12}^1 & 1 & 0 \\ C_{21}^1 & C_{22}^1 & 0 & 1 \\ \vdots & \vdots & \vdots & \vdots \\ C_{11}^N & C_{12}^N & 1 & 0 \\ C_{21}^N & C_{22}^N & 0 & 1 \end{pmatrix} \times \begin{pmatrix} B_{c,x} \\ B_{c,y} \\ B_{\text{mast},j} \\ B_{\text{mast},k} \end{pmatrix} = \begin{pmatrix} B_{o,j}^1 \\ B_{o,k}^1 \\ \vdots \\ B_{o,j}^N \\ B_{o,k}^N \end{pmatrix}, \tag{6}$$

where N is the number of observations during each mast rotation, C^i is the rotation matrix for the i th observation derived by using equation (2) and \mathbf{B}_o^i is a 2×1 vector of the measured horizontal component for the i th observation. We only consider the horizontal components because the rotations take place in the horizontal plane and thus the vertical component of \mathbf{B}_c and \mathbf{B}_{mast} cannot be decoupled in this case. The four variables that can be calculated by the minimization are $B_{c,x}, B_{c,y}, B_{\text{mast},j}$ and $B_{\text{mast},k}$, which give the horizontal components of the combined field (the vector sum of \mathbf{B}_{Mars} and \mathbf{B}_{body}) and the mast field.

We applied this method to calculate \mathbf{B}_c (the vector sum of \mathbf{B}_{Mars} and \mathbf{B}_{body}) at each of the 16 Zhurong locations in addition to the along-track calibration on 5 January. That is, the measurements from 16 mast rotations give us 16 values of \mathbf{B}_c (Extended Data Fig. 1). The field component variations of 16 measurements are consistent with the modelled rotation vectors in the horizontal plane ($B_j - B_k$ plane). There is good agreement between hodographs of combined horizontal fields at the 16 observation points and the model-predicted circles of rotating \mathbf{B}_c (Extended Data Fig. 2d). Differences in the roundness of above 0.82 (where the roundness of a perfect circle is 1) are probably due to the spatial gradient of \mathbf{B}_{body} within the rotation plane of the sensor, corresponding to a value up to 7.37 nT in the rotation plane.

In the second step, when the mast conducts at least another two rotations with different rover yaw angles at a fixed location, \mathbf{B}_{Mars} and \mathbf{B}_{body} can be decoupled according to

$$\mathbf{B}_c = C_{\text{M2R}} \times \mathbf{B}_{\text{Mars}} + \mathbf{B}_{\text{body}}, \tag{7}$$

where

$$C_{\text{M2R}} = \begin{bmatrix} \cos \omega & \sin \omega & 0 \\ -\sin \omega & \cos \omega & 0 \\ 0 & 0 & 1 \end{bmatrix} \tag{8}$$

is the transformation matrix from the geographic coordinates of Mars to the rover coordinates, and ω corresponds to the yaw angle of the rover. Under these circumstances, both \mathbf{B}_{Mars} and \mathbf{B}_{body} can be considered as constants. \mathbf{B}_{body} can be acquired by solving equation (7) with different C_{M2R} and the corresponding \mathbf{B}_c at the fixed location using the similar method as for equation (1). Thus, $\mathbf{B}_{\text{body}} = (65.6 \pm 0.8 \text{ nT}, -82.6 \pm 1.1 \text{ nT})$ in the rover frame and $\mathbf{B}_{\text{Mars}} = (-11.2 \pm 0.5 \text{ nT}, -6.2 \pm 0.6 \text{ nT})$ in the north-east-centre (NEC) frame were determined (Supplementary Table 3). As an independent check, \mathbf{B}_{Mars} can also be determined directly from this same rover rotation (and no mast rotation, shown in Supplementary Table 4) because the vector sum of \mathbf{B}_{mast} and \mathbf{B}_{body} stays constant in the sensor frame. The \mathbf{B}_{Mars} determined by these two procedures ($\mathbf{B}_{\text{Mars},x} = -11.2 \pm 0.5 \text{ nT}, \mathbf{B}_{\text{Mars},y} = -6.2 \pm 0.6 \text{ nT}$ for the two-step mast rotation method and $\mathbf{B}_{\text{Mars},x} = -10.9 \pm 0.5 \text{ nT}, \mathbf{B}_{\text{Mars},y} = -6.1 \pm 0.6 \text{ nT}$ for the first two rover rotation) were quite consistent in both direction and strength, indicating that the two-step method was valid. The substantial difference of the Martian field ($\mathbf{B}_{\text{Mars},H} \approx 7.2 \text{ nT}$) determined by the third

and the first two rover yaw rotations was possibly due to the different external field contribution, which was not reflected in the errors associated with the individual measurements. In addition, the difference in \mathbf{B}_{Mars} between the two methods was likely from the variations of the external field during the along-track calibrations (about 1 h duration). Another magnetic source might come from the spatial uniformity of the rover-generated magnetic fields during rotation of the mast, though the influence may not be large due to the small displacement of the sensor 2 centre.

The body field acquired during the along-track calibration was used to calculate \mathbf{B}_{body} at the 16 detection locations. Although the RoMAG measurements at the 16 locations were performed following the same sequence, the temperatures and the solar array currents had considerable effects on the measurements because they were made at different local times and the batteries were in different charging stages. Such influences of the temperatures and solar array currents on measurements were also found in magnetic fields of InSight IFG data³². We developed a similar algorithm to evaluate the interferences from different solar array currents at different locations to account for the variations of \mathbf{B}_{body} . To be specific, we quantitatively analysed the correlation between the measurements and the solar array currents (I_A , I_B and I_C), as well as the temperatures at the sensor (T_S) and in the electronics unit (T_E , the temperature sensor was pasted on the printed circuit board of the electronic unit). Supplementary Fig. 1 shows a 90 min time series of three components of the top-sensor measurements in the rover coordinate and the corresponding solar array currents and temperatures. During this time interval, the magnetometers were the only instruments that were switched on. The magnetic field components changed by more than 100 nT. I_A decreased by about 2 A, while I_B changed by less than 0.2 A and I_C did not change during this period. We found that the coefficient between fitting results and the observation was smaller when utilizing both I_A and I_B than when using I_A alone. Therefore, we only used I_A to calibrate the magnetic field measurements in this study. Although the temperature dependence might not be linear over a wide range of temperatures, the linearity is justified over such a small temperature range (where T_S went from -38°C to -29°C and T_E increased from 1°C to 15°C). Thus, it is reasonable to assume that the magnetic field measurements of each component were linearly dependent on I_A , T_S and T_E . Each component of the measurements can be expressed as

$$B_i = C_{1,i} + C_{2,i}T_S + C_{3,i}T_E + C_{4,i}I_A, \quad (9)$$

where the C 's are the coefficients to be determined by the multiple linear regression and i corresponds to each component. The fitting coefficients for each component are listed in Supplementary Table 5.

Supplementary Fig. 2 shows scatter plots between the observed magnetic fields and the fitting results based on the fitting coefficients. It was shown that the observed magnetic fields linearly depended strongly on the combination of temperatures and solar array currents. The correlation coefficients reached more than 0.99, with an r.m.s. of 2.2 and 2.4 nT for the \mathbf{B}_x and \mathbf{B}_y component, respectively. It was reasonable to assume that the only interferences resulting the solar array currents were contained in \mathbf{B}_{body} . The influences of the temperatures on the measurements were mainly contained in \mathbf{B}_{mast} and removed in step 1. This is because the effect of the sensor and electronic temperatures on the magnetometer recording is independent of the orientation of the sensor axis. When the mast rotates, the horizontal magnetic field components due to the un-calibrated temperature effect do not change in the sensor frame as long as the temperature remains constant during the rotation. If interference due to temperature is contained in the body field, the two horizontal components will remain unchanged during the mast rotation. On the other hand, the solar array, which is fixed to the rover body, will form a spatial magnetic field distribution and the horizontal components will exhibit a time variation with a

sine/cosine-like form in the sensor frame as the sensor rotates with the mast. Therefore, the linear correlation coefficient of I_s was used to calibrate \mathbf{B}_{body} for the 16 locations on the basis of the solar array current differences between the period of the 16-mast rotation and the along-track calibration.

We made an error estimation for the Martian field according to error propagation analysis for each step. According to equation (7), the Martian field can be expressed as

$$\mathbf{B}_{\text{Mars}} = C_{\text{R2M}} \times (\mathbf{B}_C - \mathbf{B}_{\text{body}}), \quad (10)$$

where \mathbf{B}_C and \mathbf{B}_{body} are the combined field and body field in the rover coordinates, respectively. C_{R2M} denotes the transformation from the rover to the Martian NEC coordinates. According to the law of uncertainty propagation, the uncertainties in the final Martian fields can be written as

$$\sigma_{\mathbf{B}_{\text{Mars}}} = C_{\text{R2M}} \sqrt{\sigma_{\mathbf{B}_C}^2 + \sigma_{\mathbf{B}'_{\text{body}}}^2 - 2\sigma_{\mathbf{B}_C \mathbf{B}'_{\text{body}}}}, \quad (11)$$

where $\sigma_{\mathbf{B}_C}$, $\sigma_{\mathbf{B}'_{\text{body}}}$ and $\sigma_{\mathbf{B}_C \mathbf{B}'_{\text{body}}}$ are the root mean square error (r.m.s.e.) of \mathbf{B}_C , $\mathbf{B}'_{\text{body}}$ and the covariance of the two variables, respectively. The r.m.s.e. of \mathbf{B}_C was the fitting error in step 1 (Extended Data Fig. 2e), being calculated as

$$\text{r.m.s.e.} = \sqrt{\frac{\sum_{i=1}^N (x_i - x_i^o)^2}{N}}, \quad (12)$$

where x_i and x_i^o denote the observation and fitting results (circles). This indicates the degree of deviation from the circle.

A similar method was also used to estimate the errors in step 2, in which \mathbf{B}_{body} was derived during the along-track calibration. However, before applying the \mathbf{B}_{body} in the 16 explorations, we calibrated $\mathbf{B}'_{\text{body}}$ according to the solar array currents differences as follows:

$$\mathbf{B}'_{\text{body}} = \mathbf{B}_{\text{body}} + C_{4,i}\Delta I, \quad (13)$$

where $\mathbf{B}'_{\text{body}}$ and \mathbf{B}_{body} are the body field of the 16 explorations and the along-track calibration, respectively. $C_{4,i}$ are the fitting coefficients in equation (9) of the corresponding components. ΔI are the solar array currents differences between the 16 explorations and the along-track calibration. We first determined the uncertainties of $C_{4,i}\Delta I$ as

$$\sigma_{\text{CI}} = |C_{4,i}\Delta I| \sqrt{\frac{\sigma_{C_{4,i}}^2}{C_{4,i}^2} + \frac{\sigma_{\Delta I}^2}{\Delta I^2}}, \quad (14)$$

where $\sigma_{C_{4,i}}$ and $\sigma_{\Delta I}$ are the uncertainties of $C_{4,i}$ and ΔI , respectively. The uncertainties of $\mathbf{B}'_{\text{body}}$ then can be expressed as

$$\sigma_{\mathbf{B}'_{\text{body}}} = \sqrt{\sigma_{\mathbf{B}_{\text{body}}}^2 + \sigma_{\text{CI}}^2}. \quad (15)$$

Substituting $\sigma_{\mathbf{B}'_{\text{body}}}$ into equation (11), we can obtain the final uncertainties of \mathbf{B}_{Mars} . Extended Data Fig. 3 summarizes the flowchart that describes each calibration step along with the uncertainty propagation. The Martian surface magnetic fields \mathbf{B}_{Mars} at the 16 observations were easily determined by subtracting \mathbf{B}_{body} from the combined field \mathbf{B}_C at the corresponding observation site. The calibrated values of \mathbf{B}_{body} and hence \mathbf{B}_{Mars} are shown in tabular form in Extended Data Fig. 4. The final $\mathbf{B}_{\text{crust}}$ along with the uncertainties was acquired by subtracting the external fields estimated from InSight observations from \mathbf{B}_{Mars} .

Estimation of the ionospheric contribution at the Zhurong landing site

The diurnal variations of the surface magnetic field were reported based on the InSight magnetic measurements, and the typical

peak-to-peak amplitude of the variation in a sol on each component is usually less than 30 nT (refs. 9,33,34).

To assess the magnetic field contributed by the diurnal variations mainly produced by Mars' ionospheric currents above the Zhurong rover, we made a comparison by modelling the ionospheric currents over the Zhurong and InSight landing sites and their resulting surface magnetic fields based on the model developed in ref. 35. The average intensity ratio of the modelled surface magnetic field between Zhurong and InSight, along with the measurements at InSight with the same solar longitudes (Ls), was used to estimate the ionospheric current distribution at the 16 observation locations. Although the ionospheric current pattern and its sol-to-sol variability at the Zhurong landing site may be different from those at the InSight landing site owing to their different plasma and neutral environments, we can make an overall comparison of their average intensities. The magnetic field inputs for the model were from MAVEN spacecraft measurements. The background magnetic fields used in the model are from MAVEN spacecraft measurements between 2014 and 2020. Since the magnetic fields above the InSight and Zhurong landing sites vary with local times and altitudes (ref. 33 and Supplementary Fig. 3), we calculate mean values of a 10° area in the N–S and E–W directions at each local time (24 local times in total) as the input background magnetic fields. The magnetic fields at each altitude are the averaged values in 2 km intervals (from 130 km to 280 km).

We divided the MAVEN magnetic field measurements from 2014 to 2020 above the Zhurong and InSight landing sites by local time (24 bins) and altitude (from 130 km to 280 km with a 2 km interval). We used the mean values of 10° area in each direction as the model input in the dynamo region (Supplementary Fig. 3). The neutral winds, neutral densities, and electron density above the Zhurong landing site were from the Mars Climate Database (MCD 5.3)³⁶. The electron temperature was constructed by fitting the hyperbolic tangent function with a lower and upper boundary of 510 and 3,140 K, respectively³⁷. The input parameters above the InSight landing site were from the same data sets as used in ref. 35. We predicted the surface field by assuming the ionospheric current distribution as a steady-state current sheet with large extent in horizontal direction and finite thickness. The surface field was independent from the distance from the sheet and could be given by $B_{\text{surface}} = \mu_0 \sum j(z) \cdot \frac{1}{z}$, where $j(z)$ is the current density. This assumption will result in an upper limit of the surface field estimation. On the other hand, a line current assumption will lead to a lower limit of the field estimation. The real geometry, of course, lies in an intermediate state. Both the line current and current sheet geometry assumptions were also conducted to estimate the surface field at the InSight landing site³³. Supplementary Fig. 4 shows a comparison of the modelled mean horizontal (H) components as a function of Ls. It was shown that the average intensity of the H component at the Zhurong landing site was about 83% of that at the InSight landing site during Ls 54–95° (shadow area). This intensity ratio, along with the diurnal variations from InSight IFG observations, was used to evaluate the external fields at the 16 exploration locations.

Next, we investigated the diurnal variations at InSight with respect to local true solar time (LTST) and Ls to evaluate the diurnal fluctuations as well as the sol-to-sol variations within Ls from 54° to 95° (Supplementary Fig. 5). It was shown that the median amplitude during the LTST of interest was less than 15 nT (Supplementary Fig. 5a). The peak amplitudes of H component show variations from 10 to 25 nT during Ls from 54° to 95° (Supplementary Fig. 5b). The peak amplitude, to some extent, represented the upper limit of the amplitude of a sol in the LTST of interest. The standard deviation of the peak amplitudes of B_{H} is about 3.5 nT, which can be treated as the sol-to-sol variability in B_{H} . This could be due to the sol-to-sol variations of the ionospheric currents since both the Thermospheric Neutral Wind³⁸ and/or the electron densities^{39,40} in the Martian ionosphere appear to have sol-to-sol variations. According to the ionospheric current modelling at both Zhurong and InSight, the

sol-to-sol variations at Zhurong would also be less than 3.5 nT during the Ls of interest.

We then subtracted 83% of the mean value (north and east component of ionospheric origin, $B_{\text{iono,N}} = 3.69$ nT, $B_{\text{iono,E}} = -3.8$ nT) between 10:00 and 16:00 LTST (the interval during which most of Zhurong's measurements were made) observed by InSight at the corresponding Ls from the \mathbf{B}_{Mars} observed by Zhurong to obtain the pure crustal fields from location to location. We used the mean value because the differences in the magnetic field variations in a sol as well as sol-to-sol between the Zhurong and InSight landing sites may be considerable owing to their different ionospheric plasma environments. In addition, they were not measured at the same time. We therefore used the mean values observed between 10:00 and 16:00 LTST as a proxy for the external fields at Zhurong. The standard deviation in our estimate of the external field was used, via standard error propagation, to calculate the uncertainties in our derived values of $\mathbf{B}_{\text{crust}}$. Note that the uncertainties in $\mathbf{B}_{\text{crust}}$ due to ionospheric contributions are not completely accounted for in the individual measurements. The $\mathbf{B}_{\text{crust}}$ and the corresponding uncertainties are shown in the two right columns of Extended Data Fig. 4.

By assuming that the uncertainties in each location obey a normal distribution, we calculate the fraction of the area under each normal curve of the 16 measurements that falls between –5 and 5 nT to indicate whether the possibility of no detectable crustal field exists along Zhurong's traverse. We chose the range of –5 to +5 nT because the average uncertainty of the calculated crustal fields was close to 5 nT. The average probabilities of the 16 curves, which lie in the range between –5 and +5 nT (shadow area) are 21% and 34% for the N–S and E–W component, respectively (Supplementary Fig. 6).

Defining the stratigraphy beneath the landing site

The surface regolith layer of the landing area is composed of pulverized loose materials. Some craters would penetrate through the regolith layer, excavate and emplace larger boulders on the surface. As a result, depending on whether or not rocky materials are present in the crater ejecta, the crater excavation depth (roughly 0.084 times the crater diameter) can constrain the thickness of the regolith layer⁴¹. We identified ten rocky and ten non-rocky craters with mean diameter between 7 and 82 m in HiRISE images near the landing site and estimated the average regolith thickness to be ~3 m. When catastrophic flooding carrying sediments or younger lava flows resurfaced older units, smaller craters with smaller rim heights would be buried and thus become invisible. This leaves a kink in the measured crater size–frequency distribution in the region, and the diameter of the crater at the kink should correspond to the largest crater whose rim height is equal to the lava flow thickness. In this study, we found the crater diameters that produced the kink in the crater size–frequency distribution to be between ~0.41 and 1.2 km, corresponding to a thickness of the infilling Amazonian materials of around 30–50 m based on the equations in ref. 42. There is a 24.9-km-sized ghost crater near the landing site¹⁸. The estimated thickness of the filling materials is around ~297 m. It has been hypothesized that the ghost craters have been mostly filled with VBF materials, thus the thickness of the VBF at the landing site is at least 297 – 50 – 3 = 244 m. Estimating the thickness of the Hesperian lava flows at the landing site is challenging as there are no obvious exposed basaltic materials exposed by impact detected by orbital remote sensing observations. A similar challenge is presented by estimating the thickness of the hydrated materials overlying the Noachian basement. Here, we adopted an average thickness of the Hesperian lavas of 1–2 km and a depth of the hydrated mineral layer overlying the Noachian basement of around 4–5.5 km, on the basis of a previous study⁴³.

A ghost crater, centred at 25° 6' N, 109° 54' E, in Zhurong's landing region was previously identified^{12,13}. It was also recognized from the combined images from the context camera (CTX) (Extended Data Fig. 5a). We estimated a diameter of ~10 km for the ghost crater with a depth of ~1 km based on the depth–diameter ratio criterion⁴⁴.

Magnetized layer forwards modelling

We construct a forwards model from a homogeneously magnetized layer with a cylindrical hole placed in the layer representing the Hesperian lava penetrated by a crater where the Zhurong rover is located (Extended Data Fig. 5b). The hole has a diameter and a thickness of 10 and 1 km, respectively. The magnetization vector of the layer [M_N , M_E , M_Z] = [0, 0.1, 0.1] A m⁻¹ is assumed to be uniform, being less than the maximum magnetization intensity derived from the Mars Global Surveyor (MGS)-based crustal model in the Utopia Basin²⁶. The magnetized layer is placed 200 m beneath the Martian surface. We calculate the magnetic field at the Martian surface from the layer divided into 364 triangular prisms. The magnetic field from each prism is calculated based on the polygon method^{2,45}. The Martian surface field can be obtained by integrating each prism field. Similar models are also used to investigate the magnetic variations above large craters⁴⁶.

Data availability

The RoMAG data that support the findings of this study are provided as source data. The Martian crustal field used in making Figs. 1b and 4 is from the L19 model¹⁴. The image of Zhurong's landing site for Figs. 2b and 3a is from the CTX image (https://www.nasa.gov/mission_pages/MRO/spacecraft/sc-instru-ctx.html). Data sets for constructing Supplementary Fig. 5 are publicly available via the Planetary Data System at https://pds-ppi.igpp.ucla.edu/search/?t=Mars&sc=InSight&facet=SPACECRAFT_NAME&depth=1. Source data are provided with this paper.

Code availability

We use the L19 model¹⁴ to calculate the Martian crustal field at different altitudes. We have not made the codes for the calibrated magnetic data for the RoMAG onboard the Zhurong Rover because they are not prepared for open use, but we would like to provide the codes to the scientists upon request.

References

- Acuna, M. H. et al. Global distribution of crustal magnetization discovered by the Mars Global Surveyor MAG/ER experiment. *Science* **284**, 790–793 (1999).
- Blakely, R. J. *Potential Theory in Gravity and Magnetic Applications* (Cambridge Univ. Press, 1996).
- Lillis, R. J. et al. An improved crustal magnetic field map of Mars from electron reflectometry: highland volcano magmatic history and the end of the Martian dynamo. *Icarus* **194**, 575–596 (2008).
- Acuna, M. H. et al. Magnetic field of Mars: summary of results from the aerobraking and mapping orbits. *J. Geophys. Res. Planet.* **106**, 23403–23417 (2001).
- Connerney, J. E. P. et al. The MAVEN magnetic field investigation. *Space Sci. Rev.* **195**, 257–291 (2015).
- Jakosky, B. M. et al. The Mars Atmosphere and Volatile Evolution (MAVEN) mission. *Space Sci. Rev.* **195**, 3–48 (2015).
- Weiss, B. P. et al. Paleointensity of the ancient Martian magnetic field. *Geophys. Res. Lett.* **35**, L23207 (2008).
- Mittelholz, A. & Johnson, C. L. The Martian Crustal Magnetic Field. *Front. Astron. Space* <https://doi.org/10.3389/fspas.2022.895362> (2022).
- Johnson, C. L. et al. Crustal and time-varying magnetic fields at the InSight landing site on Mars. *Nat. Geosci.* **13**, 199–204 (2020).
- Olsen, N. et al. LCS-1: a high-resolution global model of the lithospheric magnetic field derived from CHAMP and Swarm satellite observations. *Geophys. J. Int.* **211**, 1461–1477 (2017).
- Du, A. M. et al. The Chinese Mars ROVER fluxgate magnetometers. *Space Sci. Rev.* <https://doi.org/10.1007/s11214-020-00766-8> (2020).
- Ivanov, M. A. et al. Mud volcanism and morphology of impact craters in Utopia Planitia on Mars: evidence for the ancient ocean. *Icarus* **228**, 121–140 (2014).
- Zhao, J. N. et al. Geological characteristics and targets of high scientific interest in the Zhurong landing region on Mars. *Geophys. Res. Lett.* <https://doi.org/10.1029/2021GL094903> (2021).
- Langlais, B. et al. A new model of the crustal magnetic field of Mars using MGS and MAVEN. *J. Geophys. Res. Planet.* **124**, 1542–1569 (2019).
- Andrews-Hanna, J. C. et al. The Borealis Basin and the origin of the Martian crustal dichotomy. *Nature* **453**, 1212–U27 (2008).
- Marinova, M. M. et al. Mega-impact formation of the Mars hemispheric dichotomy. *Nature* **453**, 1216–1219 (2008).
- Tanaka, K. L. et al. The digital global geologic map of Mars: chronostratigraphic ages, topographic and crater morphologic characteristics, and updated resurfacing history. *Planet. Space Sci.* **95**, 11–24 (2014).
- Wu, X. et al. Geological characteristics of China's Tianwen-1 landing site at Utopia Planitia, Mars. *Icarus* <https://doi.org/10.1016/j.icarus.2021.114657> (2021).
- Li, C. et al. Layered subsurface in Utopia Basin of Mars revealed by Zhurong rover radar. *Nature* **610**, 308–312 (2022).
- McGill, G. E. Buried topography of Utopia, Mars – persistence of a giant impact depression. *J. Geophys. Res. Solid* **94**, 2753–2759 (1989).
- Lillis, R. J. et al. Study of impact demagnetization at Mars using Monte Carlo modeling and multiple altitude data. *J. Geophys. Res. Planet.* <https://doi.org/10.1029/2009je003556> (2010).
- Lillis, R. J. et al. Demagnetization of crust by magmatic intrusion near the Arsia Mons volcano: magnetic and thermal implications for the development of the Tharsis Province, Mars. *J. Volcano. Geoth. Res.* **185**, 123–138 (2009).
- Steele, S. C. et al. Magnetic properties of Martian basins cooled in a reversing dynamo. In *Proc. 54th Lunar and Planetary Science Conference* (Lunar and Planetary Institute and NASA, 2023).
- Gubbins, D. & Roberts, N. Use of the frozen flux approximation in the interpretation of archaeomagnetic and paleomagnetic data. *Geophys. J. R. Astron. Soc.* **73**, 675–687 (1983).
- Constable, C. G. et al. Geomagnetic-field models incorporating frozen-flux constraints. *Geophys. J. Int.* **113**, 419–433 (1993).
- Vervelidou, F. et al. Constraining the date of the Martian dynamo shutdown by means of crater magnetization signatures. *J. Geophys. Res. Planet.* **122**, 2294–2311 (2017).
- Mittelholz, A. et al. Timing of the Martian dynamo: new constraints for a core field 4.5 and 3.7 Ga ago. *Sci. Adv.* <https://doi.org/10.1126/sciadv.aba0513> (2020).
- Schubert, G. et al. Geophysics – timing of the Martian dynamo. *Nature* **408**, 666–667 (2000).
- Lillis, R. J. et al. Time history of the Martian dynamo from crater magnetic field analysis. *J. Geophys. Res. Planet.* **118**, 1488–1511 (2013).
- Auster, H. U. et al. Calibration of flux-gate magnetometers using relative motion. *Meas. Sci. Technol.* **13**, 1124–1131 (2002).
- Russell, C. T. et al. The magnetospheric multiscale magnetometers. *Space Sci. Rev.* **199**, 189–256 (2016).
- Joy, S. & Rowe, K. InSight IFG data calibration description (2019); <https://pds.nasa.gov/ds-view/pds/viewDocument.jsp?identifier=urn%3Anasa%3Aapds%3Ainsight-ifg-mars%3Adocument%3Ainsight-ifg-data-calibration-description>
- Mittelholz, A. et al. The origin of observed magnetic variability for a sol on Mars from InSight. *J. Geophys. Res. Planet.* <https://doi.org/10.1029/2020JE006505> (2020).
- Luo, H. et al. Natural orthogonal component analysis of daily magnetic variations at the Martian surface: InSight observations. *J. Geophys. Res. Planet.* <https://doi.org/10.1029/2021JE007112> (2022).
- Lillis, R. J. et al. Modelling wind-driven ionospheric dynamo currents at Mars: expectations for InSight magnetic field measurements. *Geophys. Res. Lett.* **46**, 5083–5091 (2019).

36. Millour, E. et al. The Mars Climate Database (version 5.3). In *Proc. Scientific Workshop "From Mars Express to ExoMars"* (ESA-ESAC & IAA-CSIC, 2018).
 37. Ergun, R. E. et al. Dayside electron temperature and density profiles at Mars: first results from the MAVEN Langmuir probe and waves instrument. *Geophys. Res. Lett.* **42**, 8846–8853 (2015).
 38. Roeten, K. J. et al. MAVEN/NGIMS thermospheric neutral wind observations: interpretation using the M-GITM general circulation model. *J. Geophys. Res. Planet.* **124**, 3283–3303 (2019).
 39. Withers, P. et al. Ionospheric characteristics above Martian crustal magnetic anomalies. *Geophys. Res. Lett.* <https://doi.org/10.1029/2005gl023483> (2005).
 40. Patzold, M. et al. A sporadic third layer in the ionosphere of Mars. *Science* **310**, 837–839 (2005).
 41. Melosh, H. J. *Impact Cratering: a Geologic Process* (Oxford Univ. Press, 1989).
 42. Garvin, J. et al. Craters on Mars: global geometric properties from gridded MOLA topography, In *Proc. 6th International Conference on Mars* (Lunar and Planetary Institute and NASA, 2003).
 43. Pan, L. et al. The stratigraphy and history of Mars' northern lowlands through mineralogy of impact craters: a comprehensive survey. *J. Geophys. Res. Planet.* **122**, 1824–1854 (2017).
 44. Robbins, S. J. & Hynek, B. M. A new global database of Mars impact craters ≥ 1 km: 2. global crater properties and regional variations of the simple-to-complex transition diameter. *J. Geophys. Res. Planet.* <https://doi.org/10.1029/2011je003967> (2012).
 45. Bott, M. Two methods applicable to computers for evaluating magnetic anomalies due to finite three dimensional bodies. *Geophys. Prospect.* **11**, 292–299 (1963).
 46. Nimmo, F. & Gilmore, M. S. Constraints on the depth of magnetized crust on Mars from impact craters. *J. Geophys. Res. Planet.* **106**, 12315–12323 (2001).
 47. Smith, D. E. et al. Mars Orbiter Laser Altimeter: experiment summary after the first year of global mapping of Mars. *J. Geophys. Res. Planet.* **106**, 23689–23722 (2001).
 48. Tanaka, K. et al. Geologic map of Mars: U.S. Geological Survey Scientific Investigations Map 3292. <https://pubs.usgs.gov/sim/3292/> (2014).
 49. Zuber, M. T. et al. Internal structure and early thermal evolution of Mars from Mars Global Surveyor topography and gravity. *Science* **287**, 1788–1793 (2000).
 50. Frey, H. Ages of very large impact basins on Mars: implications for the late heavy bombardment in the inner solar system. *Geophys. Res. Lett.* <https://doi.org/10.1029/2008gl033515> (2008).
- Foundation; Key Research Program of the Chinese Academy of Sciences (grant no. ZDBS-SSW-TLCO01); the Strategic Priority Research Program of Chinese Academy of Sciences (grant no. XDB41010304); the Strategic Priority Research Program of the Chinese Academy of Sciences (grant no. XDA17010403); the pre-research Project on Civil Aerospace Technologies of CNSA (grants no. D020103 and D020308); Shenzhen Science and Technology Program (grant no. KQTD20170810111725321); National Natural Science Foundation of China grants no. 42030205 and 42250101; and the Key Research Programs of the Institute of Geology and Geophysics, Chinese Academy of Sciences (IGGCAS-202102).

Acknowledgements

We thank the Ground Research and Application System (GRAS) of China's Lunar and Planetary Exploration Program for data preprocessing. We thank R. Lillis for the helpful comments on the manuscript. We also thank D. Qiao, L. Zhao, Z. Li, X. Feng, Z. Yi, L. Meng and J. Dai for their help in developing instruments and taking experiments. We also thank L. Tian, K. Zhang, K. Wang, G. Chen, K. Yuan, Z. Liu, F. Wu, J. Fan, J. Luo, T. Cao, D. Zhu and S. Hu for help with preparing figures. We thank D. Kong, Y. Lin and S. Yao for discussion. We acknowledge support from the National Key R&D Program of China (grant no. 2022YFF0503200); Macau Science and Technology Development Fund grant 0001/2019/A1; Macau

Author contributions

A.D., Y.P., Y.G. and H.W. conceived the work. Y.Z. and H.L. worked on the data processing method. H.L. provided the forwards numerical model. D.G., K.Z. and Y.J. interpreted the data. Y.P., R.Z. and C.W. supervised the research. All authors participated in writing the paper.

Competing interests

The authors declare that they have no competing interests.

Additional information

Extended data is available for this paper at <https://doi.org/10.1038/s41550-023-02008-7>.

Supplementary information The online version contains supplementary material available at <https://doi.org/10.1038/s41550-023-02008-7>.

Correspondence and requests for materials should be addressed to Aimin Du or Keke Zhang.

Peer review information *Nature Astronomy* thanks Anna Mittelholz, Robert Lillis and Matthew Fillingim for their contribution to the peer review of this work.

Reprints and permissions information is available at www.nature.com/reprints.

Publisher's note Springer Nature remains neutral with regard to jurisdictional claims in published maps and institutional affiliations.

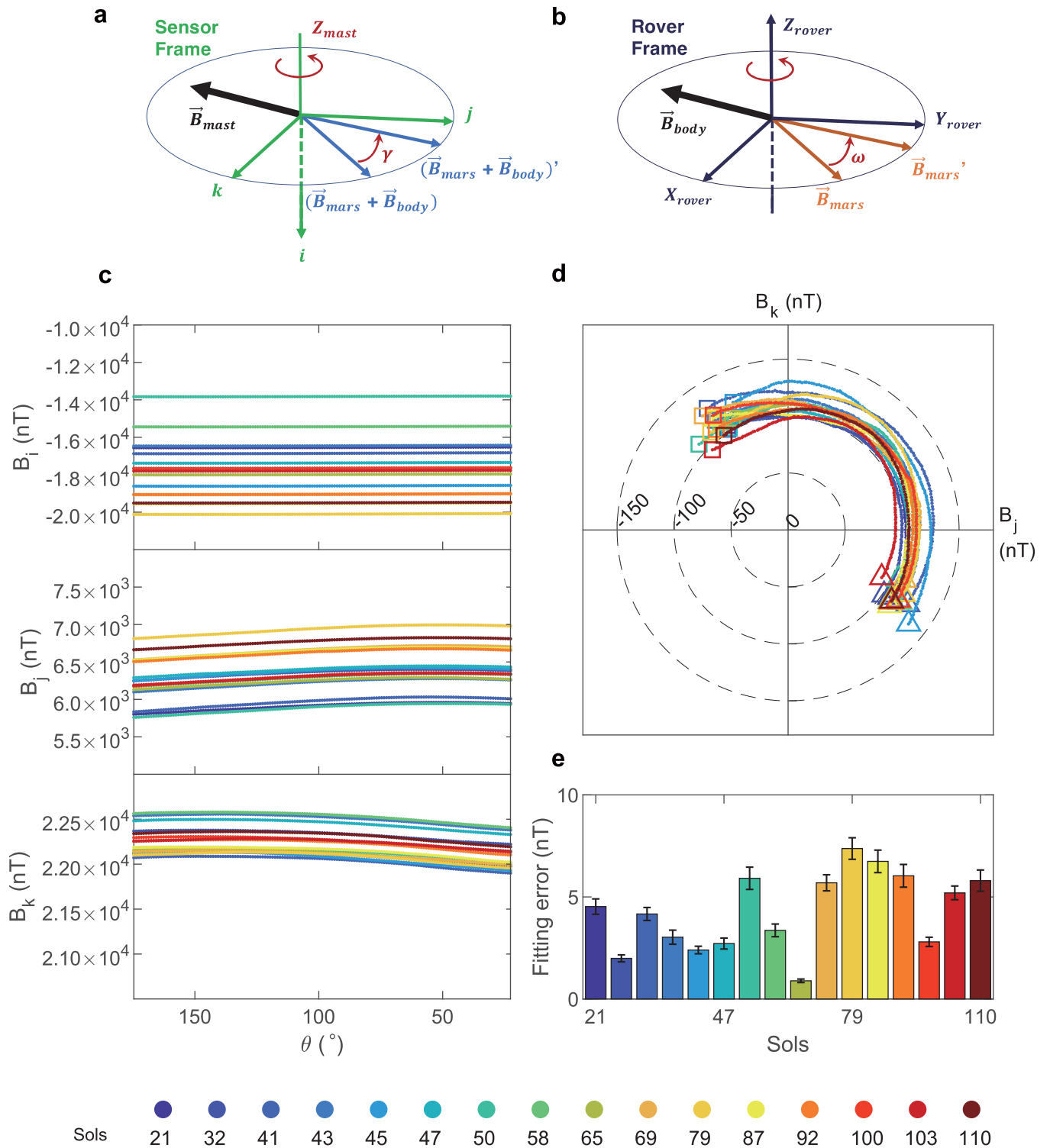
Open Access This article is licensed under a Creative Commons Attribution 4.0 International License, which permits use, sharing, adaptation, distribution and reproduction in any medium or format, as long as you give appropriate credit to the original author(s) and the source, provide a link to the Creative Commons license, and indicate if changes were made. The images or other third party material in this article are included in the article's Creative Commons license, unless indicated otherwise in a credit line to the material. If material is not included in the article's Creative Commons license and your intended use is not permitted by statutory regulation or exceeds the permitted use, you will need to obtain permission directly from the copyright holder. To view a copy of this license, visit <http://creativecommons.org/licenses/by/4.0/>.

© The Author(s) 2023

Dates	Sols	Ls (°)	LMST	X (m)	Y (m)	Z(m)	Yaw(°)	θ (°)	$B_{c,H}$ (nT)
2021-06-04	21	54.3	14:09:18	-5.1	-0.4	-0.4	107.7	196.9	103.5
2021-06-15	32	59.2	11:11:13	-115.8	-16.9	0.2	-173.7	165.2	101.1
2021-06-25	41	63.4	15:13:52	-179.2	-43.5	0.0	-153.8	230.7	125.4
2021-06-26	43	64.2	10:13:25	-184.8	-52.1	-0.0	-112.3	202.0	115.0
2021-06-29	45	65.2	16:22:51	-185.8	-54.0	-0.1	-124.4	186.9	126.6
2021-07-01	47	66.0	10:12:26	-187.9	-55.5	-0.1	-144.9	189.2	105.6
2021-07-04	50	67.4	16:21:40	-210.9	-47.0	0.1	174.3	154.0	110.7
2021-07-12	58	70.9	09:39:56	-340.6	-85.1	-0.0	170.7	196.2	112.2
2021-07-19	65	74.1	12:28:26	-443.4	-85.4	0.5	87.7	185.1	110.5
2021-07-23	69	75.9	12:27:38	-499.3	-102.9	0.8	-168.4	164.4	113.3
2021-08-03	79	80.4	12:25:46	-622.5	-55.5	3.1	172.8	175.1	117.2
2021-08-11	87	84.0	12:24:23	-690.0	-77.8	3.9	-163.5	181.4	107.7
2021-08-16	92	86.2	11:36:07	-751.9	-98.7	4.9	178.2	196.2	110.0
2021-08-24	100	89.8	11:01:45	-807.5	-184.3	5.0	-163.2	223.6	113.1
2021-08-27	103	91.2	10:54:48	-844.1	-174.7	5.8	147.1	179.5	98.0
2021-09-03	110	94.4	10:50:51	-899.9	-96.3	8.3	135.3	175.3	107.4

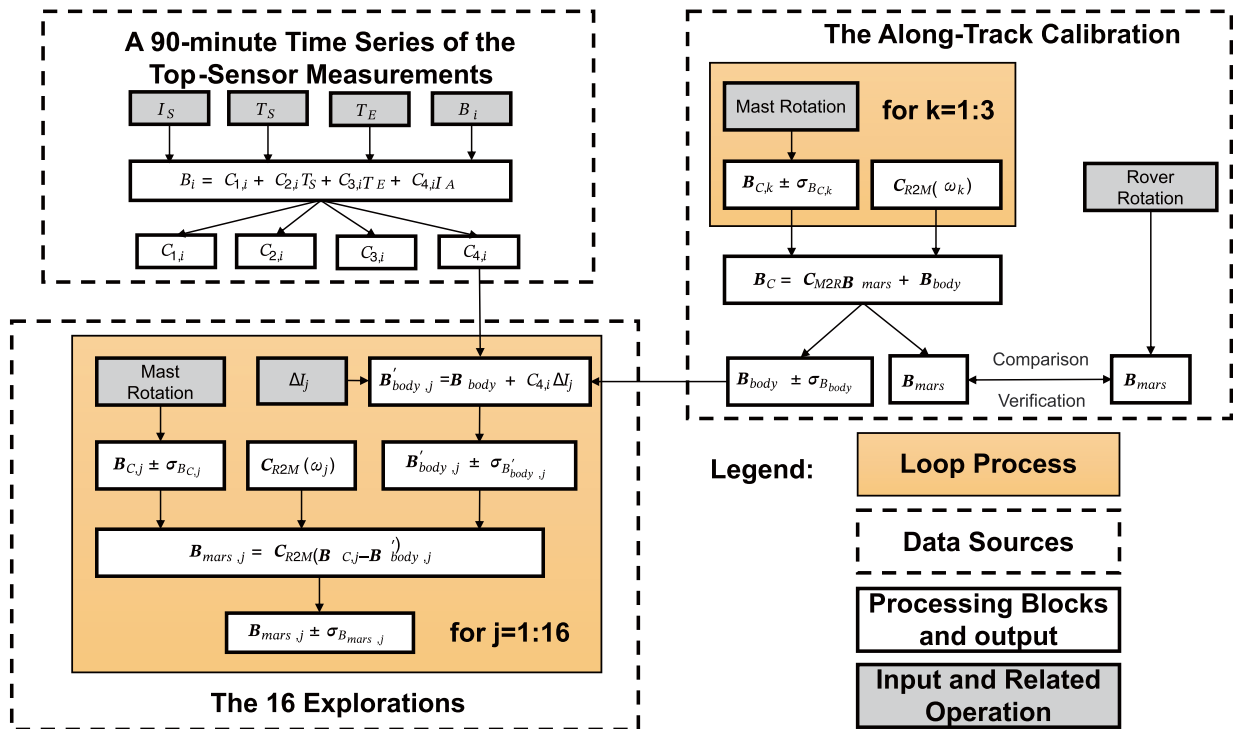
Extended Data Fig. 1 | List of Zhurong rover operation parameters during RoMAG measurements. The universal time (UT) dates, days on Mars (Sols), solar longitudes (Ls), local mean solar times (LMST) at the beginning of mast rotation, locations of the Zhurong rover relative to the lander level (LL) frame in which X

points north, Y east, and Z down, yaw angles of the rover (Yaw), rotation angles of the mast (θ), and the calculated horizontal strength of the combined field ($B_{c,H}$) are provided.



Extended Data Fig. 2 | Combined horizontal magnetic fields B_c measured during the mast rotations at 16 observation points. **a**, Sketch of the rotating combined vector $B_c = B_{mars} + B_{body}$, and the fixed field B_{mast} , in the sensor frame. **b**, Sketch of the rotating vector B_{mars}' and the body field B_{body} in the rover frame. **c**, Variations of field components along with the modeled fields (black lines) in

the sensor frame as a function of mast yaw angles during the mast rotations. **d**, Hodograph of the horizontal components of B_c on the B_j - B_k plane in the sensor frame, where the beginnings and ends of the interval are marked by squares and triangles, respectively. **e**, The mean fitting errors of the horizontal component of B_c (sample size $n = 153$) with the 95% confidence interval (error bars).

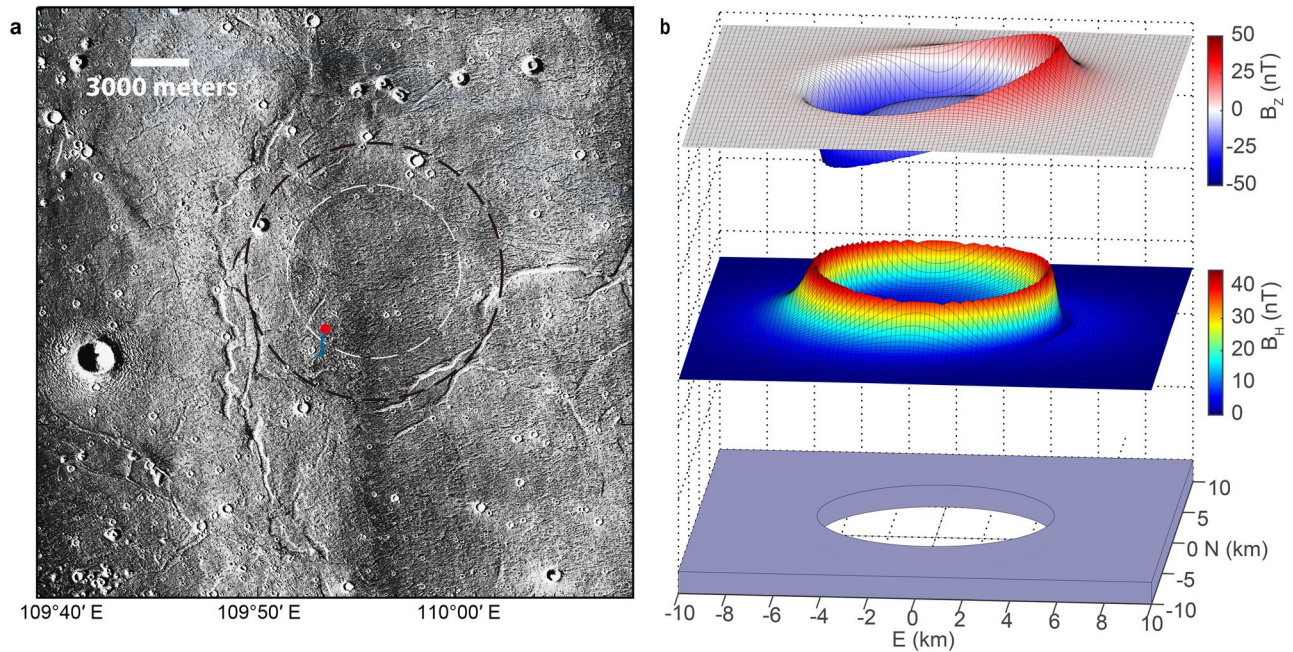


Extended Data Fig. 3 | Data processing flow chart. The combined fields (B_C) in the rover frame are determined by the mast rotation. C_{R2M} and C_{M2R} are the transformation matrices between the geographic coordinates of Mars and rover coordinate, in which ω is the yaw angle of rover. B_{mars} is the ambient field and B_{body} is the field generated by the rover body. I_A , T_S and T_E are the solar array current,

sensor temperature and electronic temperature, respectively. C are the coefficients to be determined by the multiple linear regression and i corresponds to each magnetic field component. ΔI are the solar array currents differences between the 16 explorations and the along-track calibration. B'_{body} are the magnetic fields generated by the rover body and calibrated by ΔI and C_4 .

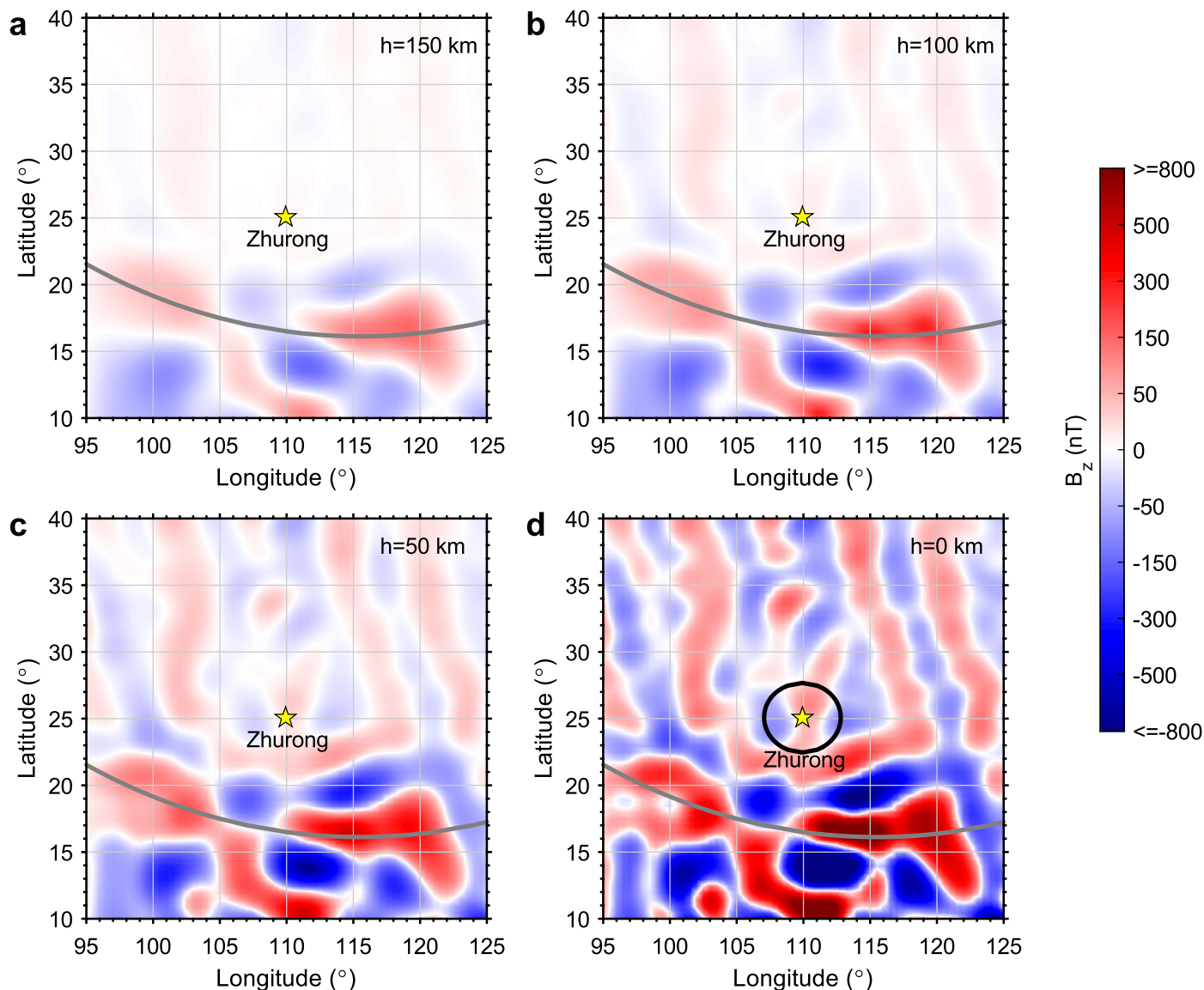
Date	Sols	$B_{\text{body, x}}$ (nT)	$B_{\text{body, y}}$ (nT)	$B_{\text{mars, N}}$ (nT)	$B_{\text{mars, E}}$ (nT)	$B_{\text{crust, N}}$ (nT)	$B_{\text{crust, E}}$ (nT)
2021-06-04	21	63.70±3.12	-82.60±1.84	-1.02±3.78	-0.32±2.41	-4.71±4.20	3.48±3.04
2021-06-15	32	64.30±3.08	-82.40±1.82	8.21±2.15	2.76±1.87	4.53±2.81	6.56±2.64
2021-06-25	41	67.70±2.93	-80.70±1.79	-16.91±2.32	11.21±3.20	-20.59±2.94	15.01±3.70
2021-06-26	43	114.50±6.82	-57.90±6.83	-1.25±3.16	24.11±7.49	-4.93±3.64	27.91±7.72
2021-06-29	45	72.50±3.20	-78.30±2.07	-20.48±1.57	27.77±2.48	-24.16±2.40	31.57±3.10
2021-07-01	47	114.90±6.93	-57.70±6.90	21.78±2.15	26.11±7.31	18.10±2.81	29.91±7.54
2021-07-04	50	70.90±3.22	-79.10±2.00	-9.71±2.57	-2.00±4.58	-13.39±3.15	1.80±4.94
2021-07-12	58	116.40±6.90	-57.00±7.04	27.50±6.52	5.44±4.70	23.82±6.77	9.24±5.05
2021-07-19	65	63.10±3.09	-82.90±1.83	9.73±1.38	-3.43±2.19	6.04±2.28	0.37±2.88
2021-07-23	69	62.50±2.99	-83.20±1.80	-12.93±2.31	-1.22±5.08	-16.62±2.94	2.58±5.41
2021-08-03	79	62.80±3.21	-83.10±1.88	-17.81±2.47	3.88±6.64	-21.50±3.07	7.68±6.89
2021-08-11	87	62.80±3.10	-83.10±1.84	-3.51±2.69	1.18±5.79	-7.19±3.25	4.98±6.08
2021-08-16	92	66.10±3.08	-81.50±1.82	-4.77±2.13	2.71±5.17	-8.46±2.80	6.51±5.49
2021-08-24	100	68.20±2.98	-80.50±1.82	-3.07±2.15	9.01±2.40	-6.76±2.81	12.81±3.03
2021-08-27	103	70.20±3.05	-79.50±1.91	-5.53±3.16	-9.21±3.32	-9.22±3.64	-5.41±3.80
2021-09-03	110	72.40±3.17	-78.40±2.05	7.06±3.97	0.20±4.11	3.38±4.36	4.00±4.51

Extended Data Fig. 4 | The calculated rover body field, Martian magnetic fields, and crustal fields along with the uncertainties, respectively. The universal time (UT) dates, days on Mars (Sols) are listed in the first two columns.



Extended Data Fig. 5 | The ghost crater in the Zhurong's landing region.
a, Combined images from Context camera (CTX: D22_035786_2060_XN_26N250W and CTX: F04_037553_2068_XN_26N250W) enhanced to better identify the ghost crater. The white and black dashed lines indicate the inner and outer rings of the double-ringed structure of a ghost crater, respectively. The Zhurong's landing site and route are denoted by the red dot and the blue

curve, respectively. The horizontal white bar indicates the scale bar of the map.
b, Modeling results of the ghost crater showing the distributions of vertical magnetic component and horizontal intensity in the top and middle panels, respectively. The cylindrical hole, which has a diameter of 10 km, corresponds to the inner ring of the ghost crater.



Extended Data Fig. 6 | The satellite-based magnetic field model (L19) and areas influenced by measurements. Panels (a–d) show maps of the horizontal intensity in the Zhurong landing region predicted by the L19 model⁶ downward continued to four different heights $h = 150$ km, 100 km, 50 km, 0 km. The corresponding vertical field strength at the Zhurong landing site (25.066° N, 109.926° E, the stars) is approximately 4.8 nT at $h = 150$ km, 9.2 nT at $h = 100$ km,

21.3 nT at 50 km, and 57.1 nT at the Martian surface. The black circle at $h = 0$ km denotes the approximate ground area averaged by the orbital model, radius 150 km. It includes some of the stronger anomalies. The corresponding circle for Zhurong's ground measurement, assuming a magnetised layer of depth 1 km, is too small to be shown on this scale. The gray curve indicates the topography boundary of Utopia basin at the surface altitude.